Journal of Materials Processing Tech. 311 (2023) 117797

Contents lists available at ScienceDirect

Journal of Materials Processing Tech.

journal homepage: www.elsevier.com/locate/jmatprotec

Towards understanding the mechanism of vibration-assisted cutting of monocrystalline silicon by cyclic nanoindentation

Weihai Huang, Jiwang Yan *

Department of Mechanical Engineering, Faculty of Science and Technology, Keio University, 3–14-1 Hiyoshi, Kohoku-ku, Yokohama 223–8522, Japan

ARTICLE INFO

Associate Editor: Adam Thomas Clare

Keywords:
Cyclic nanoindentation
Ultrasonic vibration cutting
Ductile machining
Deformation mechanisms
Brittle materials

ABSTRACT

Ultrasonic vibration cutting (UVC) is a promising technology that can promote the processing of hard-brittle materials in ductile mode. The feature of intermittent cutting in UVC is considered to promote the ductile responses of brittle materials. However, the effect of cyclic loading/impact on microscopic deformation behavior of the workpiece material in UVC is not clearly understood. This study used cyclic nanoindentation to reveal the UVC mechanism in monocrystalline silicon (Si). The surface morphology and subsurface microstructure of the residual indents were characterized and compared with those of the UVC-machined grooves. This work attempted to correlate the tool-workpiece contacts for cyclic nanoindentation and vibration cutting. Cyclic nanoindentation results show that cyclic loading promotes the extent of silicon amorphization and decreases the threshold for transitioning the β–Sn phase to the bc8 and r8 phases. As the number of indentation cycles increases, the subsurface microstructure changes from the amorphous phase to the bc8 and r8 phases. In UVC, both the critical cutting depth for brittle-to-ductile transition and the degree of amorphization in cutting chips increase in comparison to conventional cutting, which matches the trend of cyclic nanoindentation results. The findings inform the chip formation and subsurface deformation mechanisms of brittle materials during UVC.

1. Introduction

Monocrystalline silicon possesses not only superior semiconductor properties but also excellent optical performance in the infrared (IR) region. Ultraprecision machining of microstructures on silicon has drawn increasing attention, because advanced optical systems require optical components having more complex shapes to improve optical performance and/or to create new functions, as outlined in the studies of Chen et al. (2016). However, the manufacture of microstructures on silicon is challenging due to the high hardness and brittleness of the material. Ultrasonic vibration cutting (UVC) is considered an inspiring technology for machining hard-brittle materials, as stressed by Moriwaki et al. (1992) and Zhang et al. (2020), because UVC can increase the cutting depth for brittle-to-ductile transition (i.e., critical depth of cut) in machining. Zhang et al. (2017) firstly investigated the machinability of silicon by elliptical vibration cutting and successfully fabricated a sinusoidal surface and dimples in ductile mode on silicon by applying an amplitude-controlled method. Wang et al. (2020a) developed a vibration cutting device which can be operated in the resonant mode for ultrasonic elliptical vibration cutting and simultaneously in the non-resonant mode to provide cutting depth modulation. By using this device, ductile texturing of dimple arrays on silicon surfaces was achieved under unchanged amplitudes of vibration trajectory. Although optimization of UVC systems is attracting industry, such as the design of longitudinal-bending vibrator (Bai et al., 2022) and flexure hinge-based vibrator (Guo and Ehmann, 2013), and the development of vibrator controller (Wang et al., 2020c) and algorithm (Hayasaka et al., 2021) for vibration amplitude control and surface texturing, the machining mechanisms of the UVC process have been an important issue for research in the decades following the first advent of UVC systems.

Moriwaki et al. (1992) suggested that the tool-workpiece separating characteristic improves the lubrication conditions between chip and tool rake face, reducing the friction at the tool rake face-chip interface. Thus, the instantaneous cutting force was reduced, suppressing the materials' brittle fracture. Zhang et al. (2012) further developed a predictive model of instantaneous force, considering the instantaneous shear angle, thickness of cut, and characteristics of friction reverse. The force model was verified using an orthogonal elliptical vibration cutting test, which was produced through programing a CNC machine tool to drive two axes of the machine tool in simultaneous motion. Nath et al. (2011)

* Corresponding author.
E-mail address: yan@mech.keio.ac.jp (J. Yan).

https://doi.org/10.1016/j.jmatprotec.2022.117797
Received 18 July 2022; Received in revised form 3 October 2022; Accepted 8 October 2022
Available online 12 October 2022

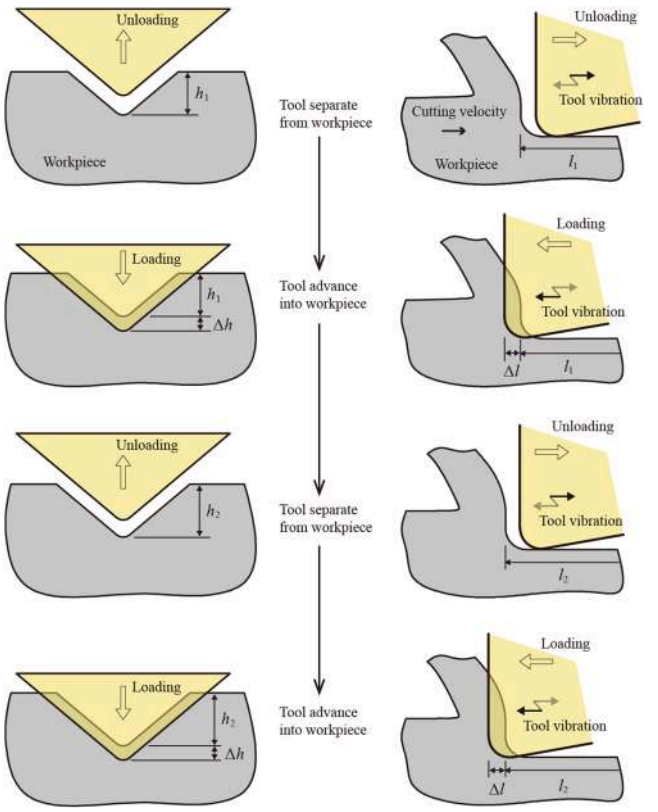

Fig. 1. Schematics of cyclic loading/unloading in (a) cyclic nanoindentation, and (b) vibration cutting.

quantitatively modeled the actual thickness of cut in an elliptical vibration cutting process, which provided a guideline for selecting proper cutting parameters, including frequency and amplitudes of tool vibration, and cutting speed. Huang et al. (2018) further analyzed the vibration trajectory in the elliptical vibration cutting process. They noticed that the fractures generated in the current locus of cut can be removed by the subsequent loci of cuts, provided the fractures do not propagate below the final machined surface. Because the final machined surface is formed by the envelope of numerous elliptical loci, and the region between the final machined surface and loci of cuts can endure fractures formation. Based on this concept, Wang et al. (2020b) optimized vibration amplitudes and cutting speed during the vibration cutting process to enhance hard-brittle material's ductile-regime cutting performance. However, the abovementioned cutting mechanisms were explored from the perspective of the tool-workpiece contact geometry and tool kinematics. The effects of vibration impact on the ductility of brittle materials, and the resulting deformation behavior of the materials were not considered.

To some extent, the deformation behavior of materials during the vibration cutting process can be revealed by simulation. For example, using a finite element simulation, Arefin et al. (2021) analyzed the stress distribution and chip formation in a linear vibration cutting process. They found that tool vibration affects strain hardening and elastic recovery of the material. Using molecular dynamics simulation, Liu et al. (2021) explored the transition of material removal behavior from extrusion to shearing related to the vibration amplitudes. Maroju and Jin (2022) proposed a mechanical model of UVC that revealed the shear angle variation was primarily affected by strain hardening of the material, and validated the proposed model using finite-element simulation. However, to date, very few studies, especially experimental studies, have focused on the material removal mechanisms of UVC processes by considering cyclic loading-induced material microstructure changes. As UVC is an intermittent cutting process, the effect of cyclic loading of cutting tools on material's mechanical properties is still unclear.

The challenge of experimental studies on the mechanisms of material removal affected by cyclic loading-induced material microstructural changes is that how the cumulative intermittent impact affects the deformation behavior of material is hard to identify directly. One solution to overcome this problem is to conduct cyclic nanoindentation tests, which can clarify the material microstructure changes due to periodic separation and contact of the workpiece and tool. This is because cyclic nanoindentation can produce periodic loading/unloading on the workpiece, which is similar to the intermittent cutting of UVC. Meanwhile, cyclic nanoindentation provides a real-time recording of load-displacement curves during the indentation process, which provides insight into the in situ deformation behavior of the workpiece material. Fig. 1 shows schematics of cyclic loading/unloading in cyclic nanoindentation and vibration cutting. In cyclic nanoindentation, the indenter presses into the workpiece at a depth of h_1 and then withdraws from the workpiece. Following complete indenter-workpiece separation, the indenter is pressed into the workpiece again at a depth of h_2, which is Δh deeper than the previous cycle. Subsequently, following the indenter-workpiece separation again, in the next cycle, the indenter is pressed into the workpiece at a depth Δh deeper than the current cycle. Similarly, in vibration cutting, the tool advances into the workpiece with a cutting distance of l_1 and then withdraws from the workpiece. Following complete tool-workpiece separation, the tool advances into the workpiece again with a cutting distance of l_2, which is Δl longer than the previous cycle. Subsequently, following additional tool-workpiece separation, in the next cycle the tool advances into the workpiece to a cutting distance Δl longer than the current cycle. When the tool enters the material (loading), the material undergoes an increasing compressive stress; next, when the tool separates from the material (unloading), the material undergoes a decreasing compressive stress; and then, the microstructure changes generated in the unloading will affect the material deformation behavior in the next loading. Clearly, there is a similarity in both the geometry and dynamics of the tool-workpiece contacts of the two processes. Although cyclic nanoindentation tests have been conducted on brittle materials, such as germanium (Gogotsi et al., 2000), silicon (Fujisawa et al., 2007), and zirconia (Juri et al., 2022), the research on connecting the findings from cyclic nanoindentation to vibration cutting process has not been reported.

This study performed cyclic nanoindentation tests and vibration-assisted groove-cutting experiments on monocrystalline silicon. The subsurface microstructural changes and surface topography of residual indents and machined grooves were examined. The effects of cyclic loading on the material microstructure change were revealed by cyclic nanoindentation. The material removal mechanisms of the UVC process considering cyclic loading-induced material microstructure change were explored by combining the cyclic nanoindentation test results with the groove-cutting experiment results. This finding may inform the fundamental research on the material deformation behavior and chip formation mechanism in the machining of brittle materials using a vibration tooling system.

2. Materials and methods

2.1. Material

The workpiece is a *p*-type single crystalline silicon (001) wafer with dimension 20 × 10 × 0.5 mm. The surface finish of the workpiece is very smooth (< 2 nm Sa) prepared by polishing process. The hardness of the workpiece is calculated to be 13.1 ± 0.1 GPa by the single cycle nanoindentation test described in the next subsection.

2.2. Cyclic nanoindentation test

Cyclic nanoindentation test was conducted on a nanomechanical test

Table 1
Setting conditions for cyclic nanoindentation.

	Total number of cycles	First cycle	Second cycle	*N* th cycle	Final cycle	Loading/unloading time (s)	
						One cycle	Total
P_{max} (mN)	1 cycle	20	–	–	20	20	20
	2 cycles	10	20	$20/2 \times N$	20	10	20
	5 cycles	4	8	$20/5 \times N$	20	4	20
	10 cycles	2	4	$20/10 \times N$	20	2	20
	20 cycles	1	2	$20/20 \times N$	20	1	20

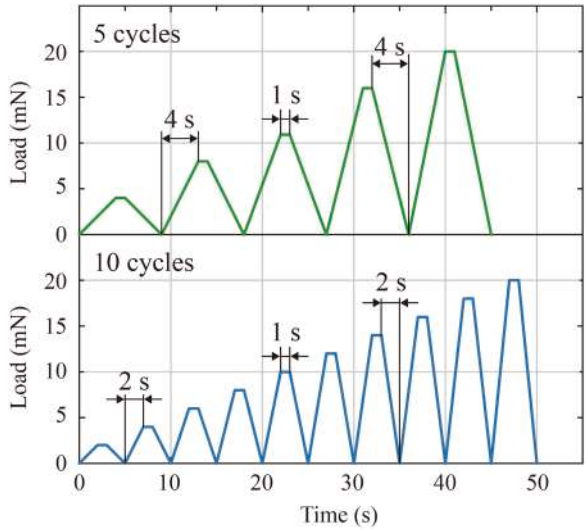

Fig. 2. Load versus time function used in 5 cycles and 10 cycles cyclic nanoindentation tests.

system (iNano® nanoindenter, KLA Corp., USA). A Berkovich-type diamond indenter with tip radius of approximately 40 nm was equipped. A single cycle nanoindentation test was conducted with a holding time of 1 s at the maximum load (P_{max}) is 20 mN. At this load, the size of residual indent approximates the spot size in laser Raman microscope, and no median cracks form in the subsurface of the residual indent, as reported by Yan et al. (2005a). The loading and unloading rates were 1 mN/s; thus, pop-out event will not occur in the single-cycle indentation with P_{max} of 20 mN, according to Jang et al. (2005). The P_{max} values of each cycle for the cyclic indentation tests are listed in Table 1. The total loading/unloading times for all the cyclic indentation tests were the same; thus, the larger the number of total cycles, the shorter the loading/unloading time for each cycle. Fig. 2 presents the load duration curves for five and ten cycles of cyclic nanoindentation. In this manner, the indenter was completely separated from the workpiece during unloading and advanced deeper into the workpiece in the following loading cycle. This process of nanoindentation can simulate the characteristics of cyclic loading/unloading during vibration cutting, as presented in Fig. 1. A 3 × 3 square array of indentations, 10 μm apart, was performed in each group of indentation tests. To avoid the influence of crystal orientation on indentation response, all the indentations were performed in the same direction where one ridge of the indenter was parallel to the [1 0 0] crystallographic direction.

2.3. Groove-cutting experiment

Fig. 3(a) presents the setup of the groove-cutting experiments. The grooves were cut by an ultraprecision lathe, which is equipped with vibration equipment (UTS2, Son-X Company, Germany). A diamond tool with a nose radius of 0.9 mm and a sharp edge was installed on the vibration equipment, vibrating at approximately 101 kHz with an amplitude of approximately 1 μm. Fig. 3(b) illustrates the groove-cutting experiment using the vibration equipment. A special jig was used to fix the workpiece, which can incline the workpiece slightly. Therefore, a progressively deeper groove can be created as the spindle rotated. After the groove-cutting experiment, the cutting direction of the microgrooves was confirmed to be along the [4 3 0] crystallographic direction. The feed rate of the X-axis slide was set to be sufficiently large such that the created grooves will not interfere with each other. The spindle speed was 20 rpm, ensuring the tool separates from the material in each vibration cycle. When the microgrooving under conventional cutting conditions, the vibration equipment was turned off.

2.4. Surface/subsurface characterization

After the nanoindentation tests, a Raman microscope was used to examine the microstructural changes of all the residual indents. The topographies of typical residual indents were observed using a scanning electron microscope (SEM), and then measured using an atomic force microscope (AFM). After the groove-cutting experiments, the microstructural changes in the cut grooves were examined using the Raman microscope. The groove's topography was characterized using a white light interferometer.

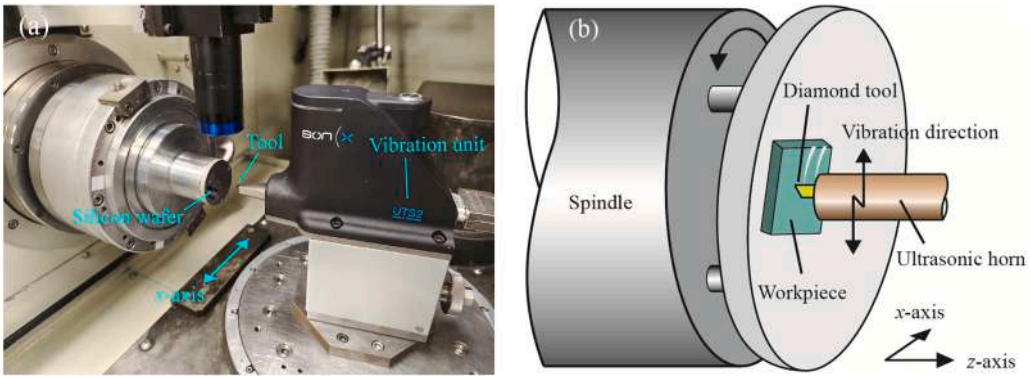

Fig. 3. (a) Experimental setup for vibration cutting; (b) illustration of groove-cutting experiment using a vibration equipment.

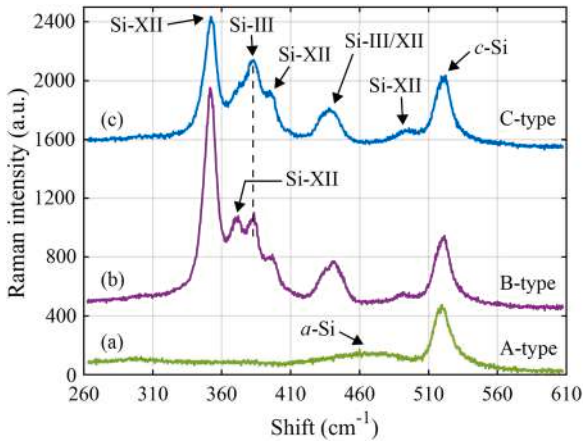

Fig. 4. Representative Raman spectra of the single-crystal silicon after cyclic nanoindentations: (a) A-type spectrum showing *a*-Si phase; (b) B-type spectrum showing Si-III and XII phases with a peak at 372 cm^{-1}; (c) C-type spectrum showing Si-III and XII phases without a peak at 372 cm^{-1}.

Table 2
Number of indents for different types of Raman spectra in different cycles of the nanoindentation test.

3 × 3 square arrays of cyclic indentation tests	Number of indentations showing phase transformation		
	A-type (*a*-Si phase)	B-type (Si-III/XII phases with the 372 cm^{-1} peak)	C-type (Si-III/XII phases without the 372 cm^{-1} peak)
1 cycle	9	0	0
2 cycles	4	2	3
5 cycles	2	4	3
10 cycles	2	3	4
20 cycles	2	2	5

3. Results and discussion

3.1. Subsurface microstructural changes of indents

The Raman spectrum of every residual indent (a total of 45 indents in five arrays) was characterized to evaluate the subsurface microstructural changes of the workpiece material after nanoindentation with different numbers of cycles. Among all the spectra, three typical types of spectra were observed, as plotted in Fig. 4. The A-type spectrum (see Fig. 4(a)) shows the formation of an amorphous phase (*a*-Si, featured by a broadband at 470 cm^{-1}) along with the original crystalline phase (*c*-Si, featured by a peak at 521 cm^{-1}), as delineated by Juliano et al. (2003). The C-type spectrum (Fig. 4(c)) shows the generation of the bc8 phase (Si-III, featured by the peaks at 382 and 438 cm^{-1}) and r8 phase (Si-XII, featured by the peaks at 352, 395, 438, and 493 cm^{-1}), along with the original crystalline phase *c*-Si, as delineated by Huang and Yan (2015) and Pizani et al. (2006). The B-type spectrum (Fig. 4(b)) shows a plot similar to that of the C-type spectrum but has one more peak at 372 cm^{-1}. Chavoshi et al. (2017) and Yan et al. (2005b) pointed out this peak corresponds to Si-XII phase. Table 2 summarizes the three types of Raman spectra of the residual indents in the indentation tests with different numbers of cycles. From Table 2 we see that all the indents produced by single-cycle indentation exhibit an A-type spectrum, showing only an amorphous phase transformation. However, as the number of indentation cycles increased, the number of indents exhibiting A-type spectrum decreased and those showing B-type and C-type spectra increased, which indicates that the amorphous phase changed to the Si-III phase and Si-XII phase through multi-cycle indentation. This result is consistent with those results reported by Huang and Yan (2015) and Pizani et al. (2006). Moreover, it can be noted that the amorphous phase almost completely transformed to the Si-III and Si-XII phases within five cycles; then, as the number of indentation cycles continued to increase, the number of indents exhibiting a B-type spectrum decreased and those showing a C-type spectrum increased. Jang et al. (2005) and Yan et al. (2005b) have reported that the amorphous state tends to form at fast unloading, whereas a mixture of Si-III and Si-XII phases forms upon a slow unloading, which is attributed to the fact that the slower unloading rates provide more time for the nucleation event to occur. However, in this study the mixture of Si-III and Si-XII phases is inclined to form when the number of indentation cycle is large; meanwhile the loading/unloading rate increases with the number of indentation cycle (see Table 1). In other words, the formation of Si-III and Si-XII phases could also occur at fast unloading. This indicates that the nucleation of Si-III and Si-XII phases occurred in the unloading period of each cycle and accumulated as the number of indentation cycles increased, eventually leading to the phase transformation. This issue will be discussed in detail in Section 4.1.

Although the number of indents showing an amorphous phase decreased with increasing indentation cycles, the amorphous phase remained in the residual indent after 20 indentation cycles. Therefore, the A-type spectra of the indents produced by the cyclic indentations of different cycles were compared, as presented in Fig. 5(a). The intensities of the main peaks, that is *c*-Si and *a*-Si peaks, of the spectral curves were extracted, as plotted in Fig. 5(b). In the first several cycles, as the number of cycles increased, the *c*-Si peak intensity dropped dramatically; then, when the number of cycles continued to increase from five to twenty cycles, the intensity drop became much lower. On the other

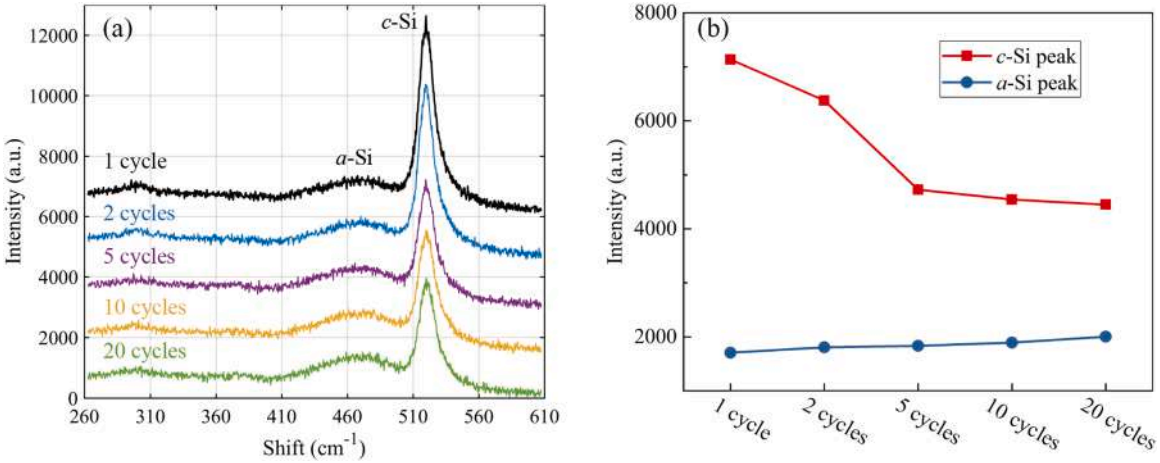

Fig. 5. Comparison of A-type Raman spectra among residual indents produced by different nanoindentations: (a) spectral curves, and (b) intensities of main peaks.

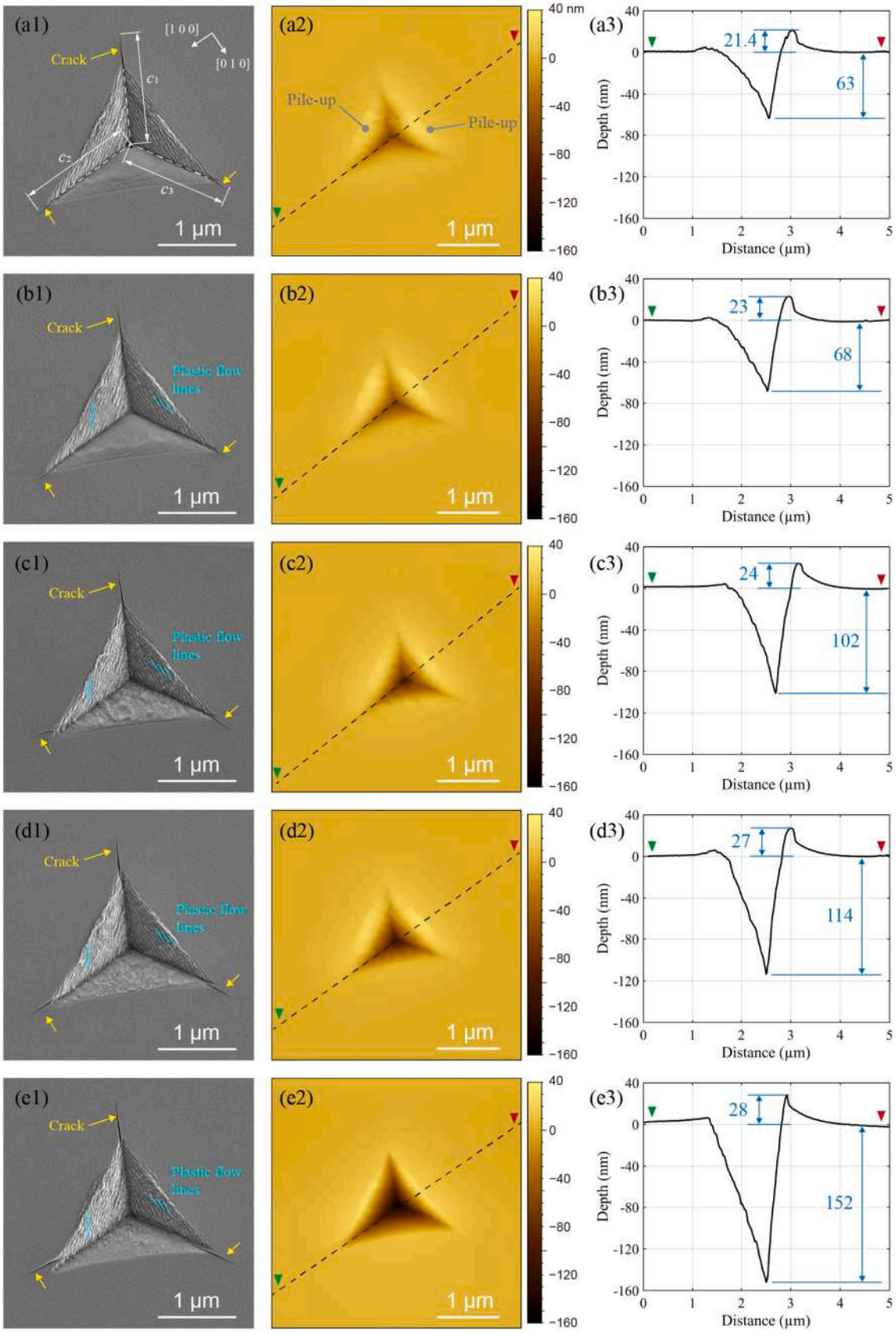

Fig. 6. SEM images of typical residual indents of: (a1) single cycle indentation, (b1) two cycles, (c1) five cycles, (d1) ten cycles, and (e1) twenty cycles cyclic indentations. The yellow arrows in (a1)–(e1) refer to the indentation-induced cracks. (a2)–(e2) are the surface topographies of residual indents measured by AFM, which correspond to the residual indents shown in (a1)–(e1), respectively. (a3)–(e3) are the cross-sectional profiles of the residual indents shown in (a2)–(e2), respectively.

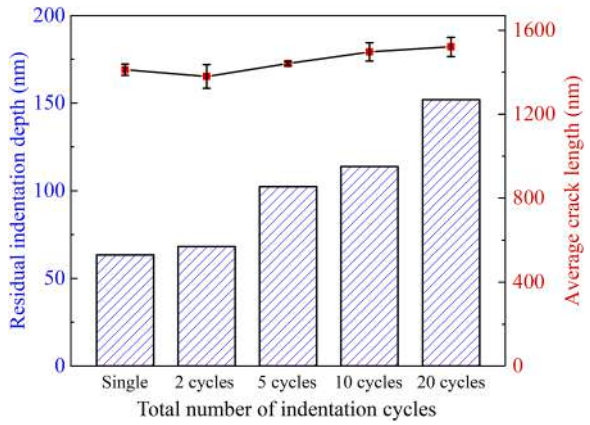

Fig. 7. Comparison of the residual indentation depth and the average crack length of the indentations with different numbers of loading cycles.

hand, the intensity of the *a*-Si peak continued to increase slightly with an increase in the number of cycles, indicating that the degree of amorphization increased with the increasing number of cycles.

3.2. Topography of indents

SEM images of the residual indents with an amorphous phase are presented in Fig. 6(a1)–(e1). All indentations caused radial cracks, which propagated normal to the surface along three corners of the residual indent. The length of each radial crack (*c*) was measured from the end of the crack at the workpiece surface to the center of the indent, as shown in Fig. 6(a1). For every indent, the average lengths of the three radial cracks were calculated and are shown in Fig. 7. The length of the crack induced by two cycles of cyclic indentation is shorter than that induced by a single cycle of indentation, and then the length of the crack increases with the number of indentation cycles. Furthermore, the lines parallel to the edges of the indent are clearly observed on two of the three sides of the indent surface, which is attributed to the compressive and shear stress-induced plastic flow of the material, as reported by Geng et al. (2021). However, owing to the slight inclination of the sample surface with respect to the horizontal plane, less deformation occurs on the lower side of the sample, and thus, no plastic flow lines appear on the lower side of the indent surface.

The corresponding surface topographies of the residual indents presented in Fig. 6(a1)–(e1) were measured using AFM, as shown in Fig. 6(a2)–(e2). It can be seen from every indentation that significant pile-ups formed next to the side of the two indent surfaces where the plastic flow lines were generated, whereas an insignificant pile-up was produced next to the side of the one indent surface without plastic flow lines. This indicates that the workpiece material beneath two of the three sides of the indenter underwent greater plastic deformation, which is consistent with the formation of plastic flow lines (Fig. 6(a1)–(e1)).

Then, the cross-sectional profiles of the residual indents were extracted to analyze the depth of the residual indents and the height of the pile-ups, as shown in Fig. 6(a3)–(e3). It can be seen from the profiles that the residual indent's depths gradually increased with an increasing number of indentation cycles. In particular, the residual indent depths of 10 and 20 cycles cyclic indentations were 1.8 and 2.4 times the residual indent depth of single cycle indentation. However, the height of the pile-ups was slightly affected by the number of indentation cycles, which increased from 21.4 nm to 28 nm when the indentation cycles increased from 1 to 20. This indicates that subsurface densification was enhanced by the cyclic indentation. Considering the presence of *a*-Si and *c*-Si in the subsurface of these residual indents, and the fact that *c*-Si can be compressed in volume at high pressures without phase transformation, as reported by Domnich and Gogotsi (2002), it is supposed that cyclic indentation caused greater residual stresses that compress the *c*-Si. Nevertheless, since the probability for the formation of Si-III/XII phases increases with the number of indentation cycles (see Table 2), and the Si-III/XII phases are denser than *c*-Si at the same pressure according to Domnich and Gogotsi (2002), it can be inferred that the material compression in relation to the phase transformation becomes dominant in the cyclic indentation as the number of indentation cycles increases. The residual depth of each indent is also plotted in Fig. 7 to perform a combined analysis of the crack length and residual indentation depth. Although the depth of the residual indents increased with an increasing number of indentation cycles, the crack length first decreased when the indentation cycle changed from 1 to 2, and then increased with an increase in the number of indentation cycles. The crack length of five cycles of cyclic indentation is slightly higher than that of single-cycle indentation, but the residual indent depth of the former is 1.6 times greater than that of the latter. Therefore, it can be inferred that incremental cyclic loading can suppress crack growth. This might be because the amorphous phase silicon gradually increases in the cyclic indentation, and thus decreases the brittleness of the material.

3.3. Load–displacement curve characteristics

To understand the evolution of the deformation behavior of materials under cyclic loading conditions, analyzing the curves of load-displacement and average contact pressure-displacement is an effective approach. In every indentation group, the load–displacement curve of a residual indent showing an A-type spectrum was plotted, as shown in Fig. 8. An artificial shift was inserted between cycles to easily observe the curve of each cycle. Meanwhile, to clearly illustrate the relationship between the curves of the former and latter cycles, several curves for two adjacent cycles were extracted from every cyclic indentation group and plotted without artificial shifts. Fig. 8(a) shows the curve of a single-cycle indentation in which an elbow event was observed upon unloading. This phenomenon is widespread in the nanoindentation of single-crystal silicon, as reported by Domnich et al. (2000) and Jang et al. (2005), indicating the formation of an amorphous phase. As the number of indentation cycles increased, the number of curves also increased; however, the shapes of the curves for each cycle (excluding the curve of the first cycle) in all groups, which have a lanceolate leaf-like shape, i.e., the widest part of the curve near the center and the narrowest part near the apex, are the same. This is because the elbow event is formed upon unloading in every indentation cycle, and the loading curve has a variable curvature.

By analyzing the curve of two adjacent cycles without an artificial shift (see the right half of Fig. 8(b)), in the former cycle, the indentation depth decreased to a minimum value when the applied force decreased to zero. In the latter cycle, at the beginning of reloading, the indentation depth increased slowly, as indicated in stage 1. As the indentation depth continued to increase, the increasing rate of indentation depth became faster (stage 2). With further increase in the indentation depth, the increasing rate of the indentation depth slowed down again, until the applied force approached the value equal to the peak load of the previous cycle (stage 3). When the applied force reached the peak load of the previous cycle, the indenter penetrated to the same depth as before the unloading of the previous cycle. This suggests that, from a macro perspective, the material underwent quasi-elastic deformation during the period from the unloading of the previous cycle to when the applied force reloaded to a value equal to the peak load of the previous cycle in the current cycle. Once the applied force exceeded the peak load of the previous cycle, the increasing rate of the indentation depth became fast again (stage 4). As the number of indentation cycles increased to 5, 10, and 20, the trend of their loading curves was the same as the two cycles of cyclic indentation, as shown in Fig. 8(b)–(e), respectively.

The load-displacement curves for the residual indents in the 10 and 20 cycles indentations that show B-type and C-type spectra, respectively, are plotted in Fig. 9. In the curve of 10 indentation cycles (Fig. 9(a)), a pop-out event occurred upon the unloading of the 9th cycle. This

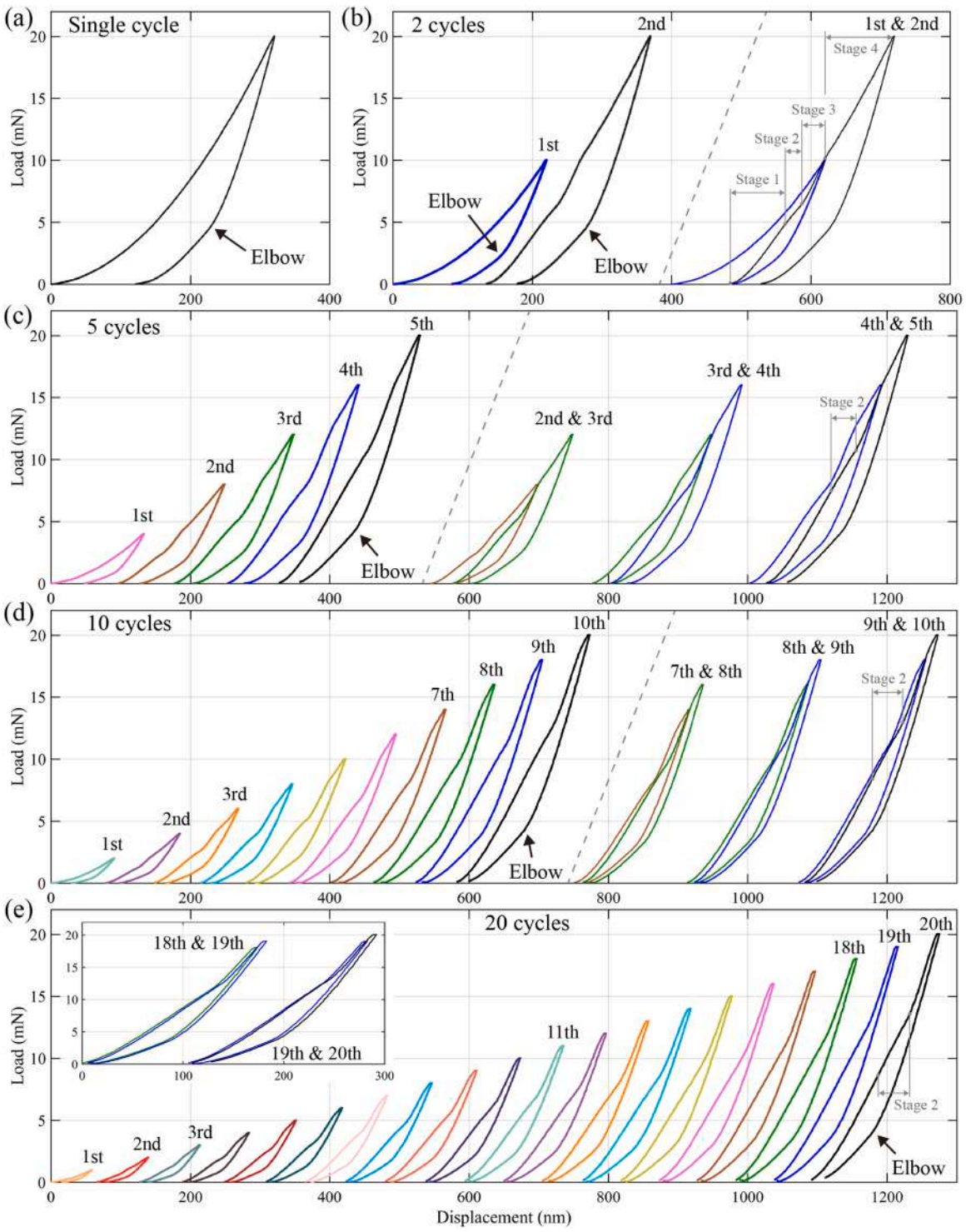

Fig. 8. Load-displacement curves of the residual indents showing A-type Raman spectrum in: (a) single cycle indentation, (b) two cycles, (c) five cycles, (d) ten cycles, and (e) twenty cycles cyclic indentations.

indicates that during the unloading process, the Si-II phase, which is transformed from *c*-Si in the loading process changes to Si-III and Si-XII phases with lower density structures, resulting in volumetric expansions, as reported by Juliano et al. (2003). In the following cycle (which is also the last cycle), a pop-out event also occurred during the unloading process but was not as clear as the previous pop-out. Similarly, in the curve of 20 indentation cycles (Fig. 9(b)), the pop-out event occurred upon the unloading of the 9th cycle, and it gradually became less noticeable as the number of indentation cycles increased. This indicates that the Si-III and Si-XII phases can complete the phase change from the Si-II phase in a few indentation cycles. Moreover, it is worth mentioning that Yan et al. (2006) reported that the load-threshold for the occurrence of a pop-out event is approximately 30 mN in single-cycle nano-indentation of single-crystal silicon. In contrast, in cyclic indentation the pop-out event occurred at a load of less than 10 mN in the 9th of the 20 cycles. Therefore, it can be inferred that the cyclic loading effect will decrease the threshold for the Si-II phase transitioning to the Si-III and XII phases.

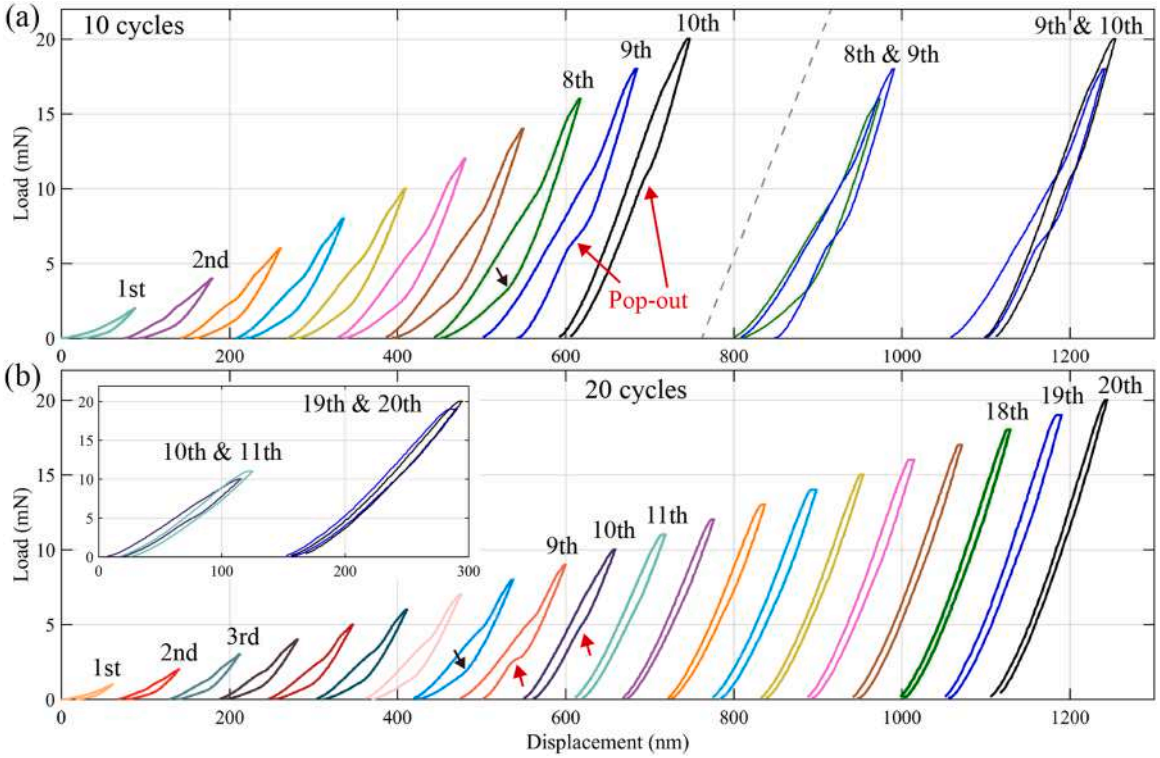

Fig. 9. Load-displacement curves of: (a) the residual indent showing B-type Raman spectrum in ten cycles cyclic indentation, and (b) the residual indent showing C-type Raman spectrum in twenty cycles cyclic indentation. The black arrows indicate the elbow event, and the red arrows indicate the pop-out event.

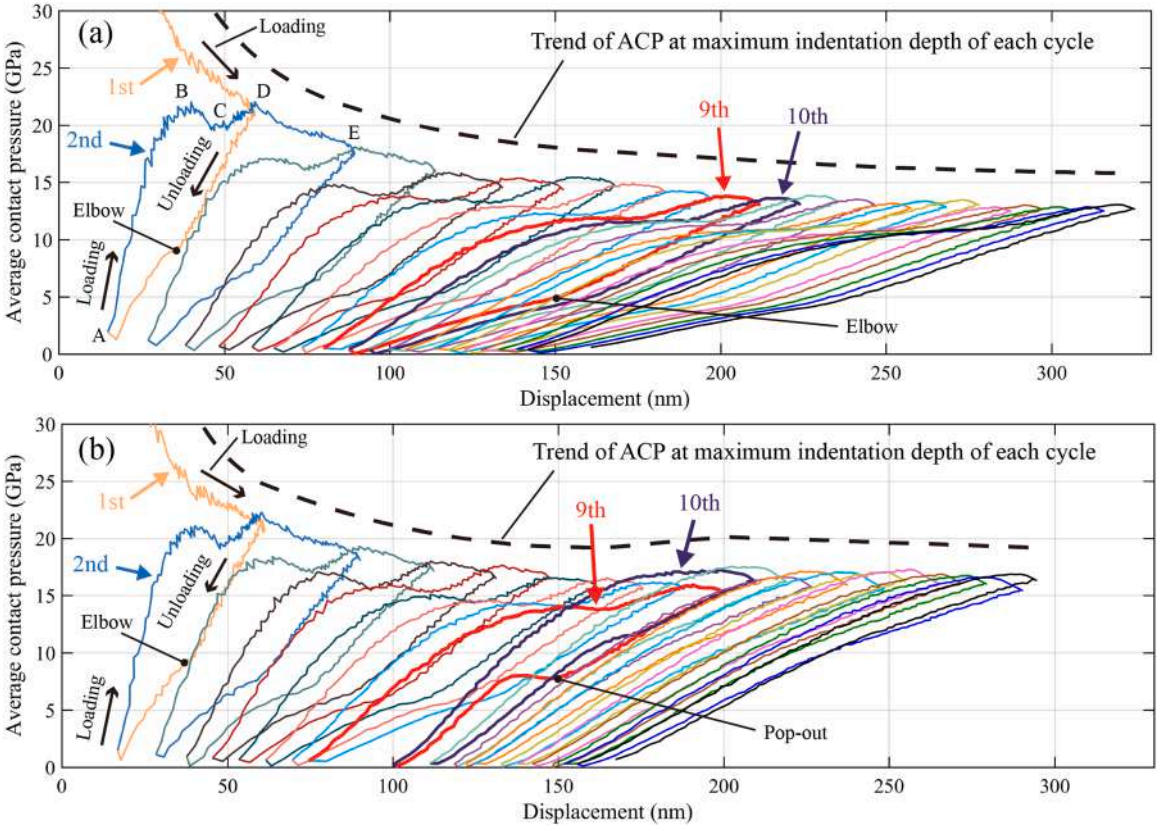

Fig. 10. Curves of average contact pressure vs. displacement calculated from the load-displacement curves of (a) Fig. 8(e), and (b) Fig. 9(b).

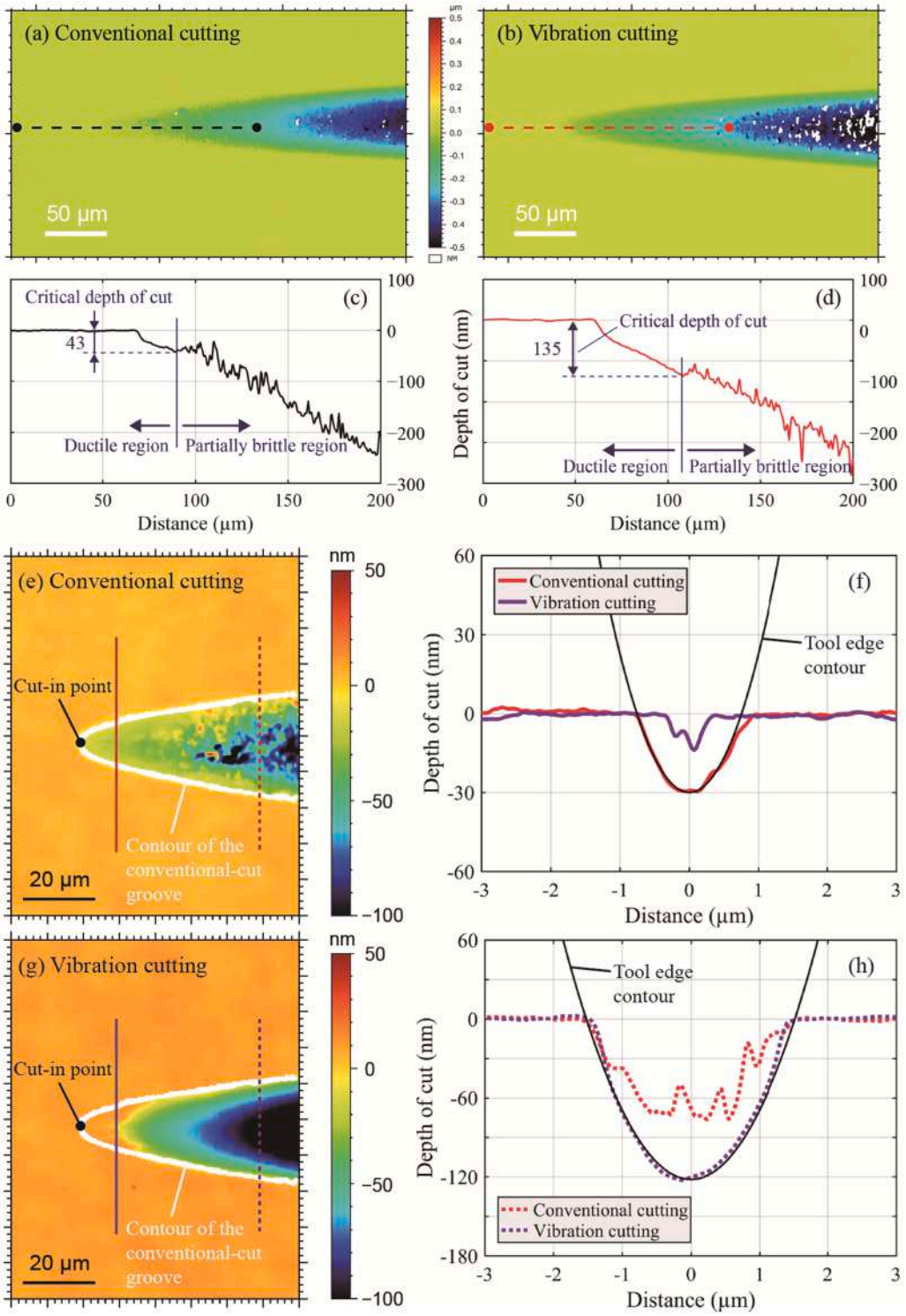

Fig. 11. 3D topographies of the microgrooves machined (a) without, and (b) with vibration assistance. Cross-sectional profiles of the microgrooves extracted along (c) black dashed lines in (a), and (d) red dashed lines in (b). (e) and (g) are the enlarged views of the cut-in area of the grooves in (a) and (b), respectively. (f) and (h) are the surface profiles along the solid lines and dashed lines in (e) and (g), respectively.

To confirm the evolution of the phase changes occurring in cyclic indentations, the curves of average contact pressure vs. displacement were calculated based on the load-displacement curves. The average contact pressure (*ACP*) is expressed as

$$ACP = \frac{P}{A} \tag{1}$$

where P is the real-time load on the indenter and A is the projected contact area under the corresponding indenter load.

According to Fischer-Cripps (2011), the value of A for a Berkovich indenter is related to the depth h_c beneath the contact, and can be calculated as follows:

$$A = 24.5 \times h_c^2 \tag{2}$$

$$h_c = h_i - h_s \tag{3}$$

where h_i is the real-time displacement of the indenter, which is recorded in the load-displacement curve. h_s is the elastic deflection of the indented surface.

h_s can be estimated by Eq. (4) according to Juliano et al. (2003).

$$h_s = (h_s)_{\max}\sqrt{\frac{P}{P_{\max}}} \tag{4}$$

where $(h_s)_{\max}$ is the elastic deflection of the indented surface when the indentation load reaches a maximum and can be calculated as follows:

$$(h_s)_{\max} = \varepsilon\frac{P_{\max}}{dP/dh} \tag{5}$$

where ε is 0.75 for the Berkovich indenter. $P_{\max}$ is the maximum load during a given indentation cycle. dP/dh is the contact stiffness, S, which is the value of the initial slope of the unloading curve of the given cycle.

Fig. 10(a) and (b) show the curves of the average contact pressure versus indentation depth calculated from the load–displacement curves presented in Figs. 8(e) and 9(b), respectively. The former indentation corresponds to the indent showing an A-type Raman spectrum (indicating the formation of an amorphous phase) after 20 cycles of cyclic indentation (hereinafter referred to as A-type indent), and the latter indentation corresponds to the indent showing a C-type Raman spectrum (indicating the formation of Si-III/XII phases) after 20 cycles of cyclic indentation (hereinafter referred to as C-type indent). From an overall perspective, the pressure at the end of the first loading period for both A- and C-type indents is ~21 GPa, which is much larger than the single-crystal silicon hardness (~13 GPa). As the load increases with the number of indentation cycles, the pressure at the end of the loading period gradually decreases. This phenomenon of the indentation depth-dependent contact pressure has been known as indentation size effect (ISE), which is related to the geometrically necessary dislocations and statistically stored dislocations in the workpiece surface, according to Nix and Gao (1998). From a micro perspective, the average contact pressure curves of the A- and C-type indents are similar in the first several cycles. In the reloading period, for example the second loading period, the contact pressure gradually increases with the indentation depth (see AB region in Fig. 10(a)), which corresponds to stage 1 in the load-displacement curve, as defined in Fig. 8(b). Then, the contact pressure suddenly decreases (see BC region), which corresponds to stage 2 in the load-displacement curve. As the indentation depth continues to increase, the contact pressure starts to increase again until the indentation depth increases to the depth equal to the maximum indentation depth of the previous cycle (see CD region), which corresponds to stage 3 in the load-displacement curve. Then, the contact pressure decreases again with further increase in the indentation depth until the unloading period begins (see DE region), which corresponds to stage 4 in the load-displacement curve. The pressure drop in the BC region has the same characteristics as the pop-in event reported by Chang and Zhang (2009), indicating that the material deformation behavior transitions from purely elastic deformation (AB region) to elastic-plastic deformation accompanied by the phase transformation from amorphous phase to Si-II phase. In the CD region, the contact pressure shows an increasing trend again, indicating that the phase transformation-based plastic deformation tends to slow down, and the elastic deformation becomes dominant again. Once the indentation depth exceeds the maximum indentation depth of the previous cycle, further plastic deformation occurs, leading to a pressure drop in the DE region, which is confirmed by Gogotsi et al. (2000).

However, in the 9th unloading period, the pressure curve of the C-type indent appears significantly different from that of the A-type indent, which is caused by the occurrence of a pop-out event in the C-type indent. Subsequently, for the C-type indent, the pressure at the end of the 10th loading period suddenly increases, and is maintained at a high value at the end of the loading period in the remaining cycles. The pressure at the end of the 20th loading period is ~16 GPa, which is larger than the single-crystal silicon hardness. This is because Si-III/XII phases are formed in the workpiece subsurface when the pop-out event occurs, which is harder than the diamond cubic structure silicon (Si-I) phase, stressed by Huang and Yan (2015). After the formation of Si-III/XII phases, the sudden pressure drop is absent in the contact pressure curve of the loading period, because the compressed Si-III/XII phases will not transform to Si-II. Nevertheless, the slope of the contact pressure gradually slows down as the indentation depth increases, and then a slight pressure drop occurs when approaching the end of loading (stage 4 in the load-displacement curve). This indicates that the Si-I phase in the deeper substrate transforms to Si-II phase. For the A-type indent, from the 1st to the 20th indentation cycle, the pressure at the end of the loading period decreases continuously to ~13 GPa, similar to the hardness of single-crystal silicon.

Based on the pressure analysis of Fig. 10(a) and (b), it is clear that before the unloading of each cycle, a certain amount of the Si-II phase will be generated beneath the indenter. When the unloading starts, the Si-II phase does not revert to the Si-I phase but instead changes to an amorphous phase. The pressure at which the amorphous phase transformation (elbow event) first occurs is ~9 GPa during the unloading of the first cycle. Furthermore, nanocrystalline grains with the r8 structure (Si-XII) nucleate within the amorphous phase when the pressure is released to ~8.2 GPa, and then some of them would convert to the bc8 structure (Si-III) when the pressure is decreased to ~2 GPa, as reported by Ackland et al. (1994). Because the amount of nucleation of nanocrystalline grains in the amorphous phase is random, a seed crystal may not have been generated even after 20 cycles of cyclic indentation. Therefore, it is possible to observe that the elbow event occurs during the unloading of every cycle, as shown in Fig. 10(a). Consequently, the residual indent shows an A-type Raman spectrum. Nonetheless, there is a trend that the greater the number of indentation cycles, the greater the possibility of producing a C-type indent. This is because the Si-XII phase is harder than the Si-I phase; thus, the nanograins of the Si-XII phase grow as the number of indentation cycles increases. It can be inferred from Fig. 10(b) that a sufficient Si-XII phase is generated as a seed crystal after eight indentation cycles. When the pressure falls below 7.8 GPa during the unloading of the 9th cycle, the Si-II phase transforms to the Si-XII phase rapidly, accompanied by volume expansion, which causes a pop-out event. As the pressure further decreases to ~2 GPa, a part of the Si-XII phase converts to the Si-III phase. When the loading of the 10th cycle starts, the Si-XII phase remains in the subsurface and the Si-III phase inverts to the Si-XII phase; thus, from the 10th indentation cycle, the pressure suddenly increases. The detailed evolution of phase transformation is discussed in Section 4.

3.4. Topography of ultrasonic vibration cut microgrooves

Fig. 11(a) and (b) show 3D topographies of the microgrooves plunge-cut without and with vibration assistance. The groove cut with vibration assistance had a more intact edge than the groove cut without vibration assistance (conventional cutting), though both grooves were cut at the same cutting parameters by using the same tool edge. Considering that chipping tends to occur at the groove edge in the microgrooving of brittle materials during conventional cutting because of the high stress concentration at the apex of the groove edge, it can be inferred that vibration cutting promotes more ductile removal behavior at the groove edges when brittle materials are microgrooved. This may be because the instantaneous cutting force could be reduced by vibration cutting, which consequently reduces the tensile stress in the workpiece, as mentioned by Moriwaki et al. (1992). Subsequently, the cross-sectional profiles of the microgrooves were extracted, as shown in Fig. 11(c) and (d), for determining the critical depths of cut where the brittle-to-ductile transition appeared. The critical depth of cut for the groove cut under conventional cutting conditions was 43 nm, while that for the groove cut

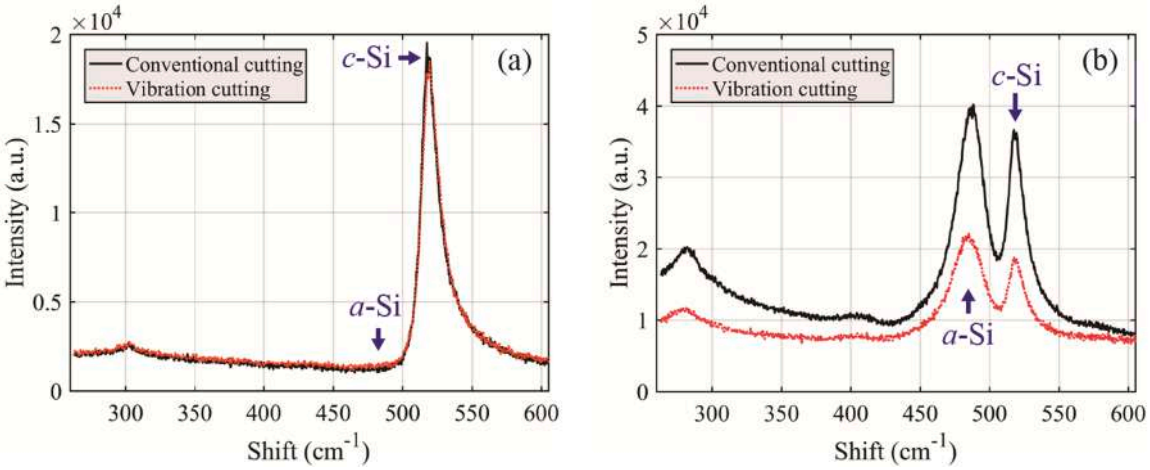

Fig. 12. Raman spectra of (a) groove surface, and (b) cutting chips.

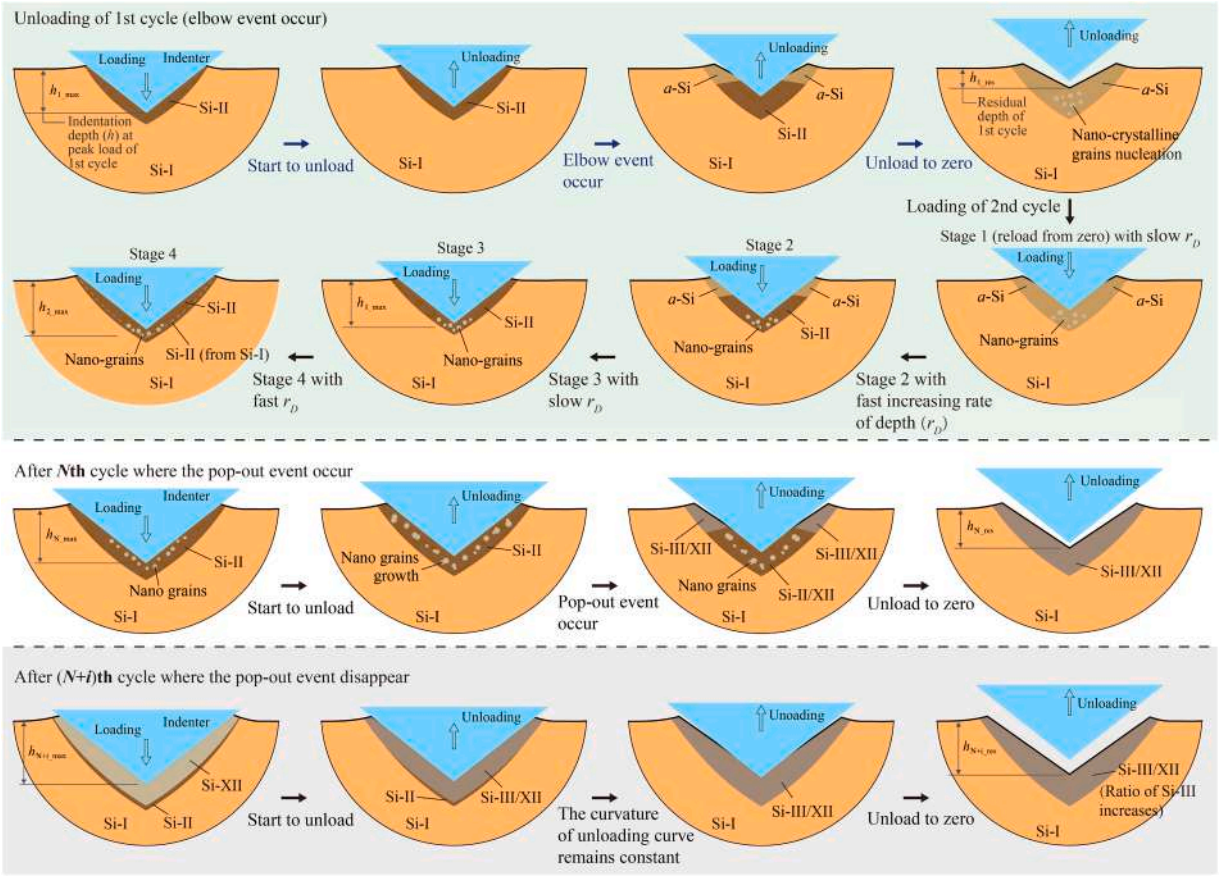

Fig. 13. Schematic model for the evolution of subsurface microstructural changes under cyclic loading condition.

under vibration-assisted cutting conditions was 135 nm. This means that the critical depth of cut increases 3-fold by using a vibration cutting device.

The enlarged views of the 3D topographies of the cut-in areas of the conventional-cut and vibration-cut grooves are presented in Fig. 11(e) and (g), respectively. Generally, in the conventional-cut groove, the smooth transition of the contour line starting from the cut-in point is very short, and many spots with various colors are observed as the groove becomes deeper. This indicates that ductile mode cutting was realized in the beginning but was limited to a very small depth of cut, which was then followed by brittle mode cutting, causing microfractures to form on the grooved surface. By contrast, in the vibration-cut groove, the smooth transition of the contour line is distributed throughout the observation area without any colored spots. This suggests that the groove in the observation area was machined in the ductile mode, and its ductile-to-brittle transition depth was much greater than that of the conventional-cut groove. However, under the vibration-assisted cutting condition (Fig. 11(g)), the material was not removed from the cut-in point, but a dozen microns from the cut-in point. Fig. 11(f) shows the cross-sectional profiles of both the conventional- and vibration-cut grooves, which are perpendicular to the cutting direction near the cut-in point. The cross-sectional profile of the conventional-cut groove fits

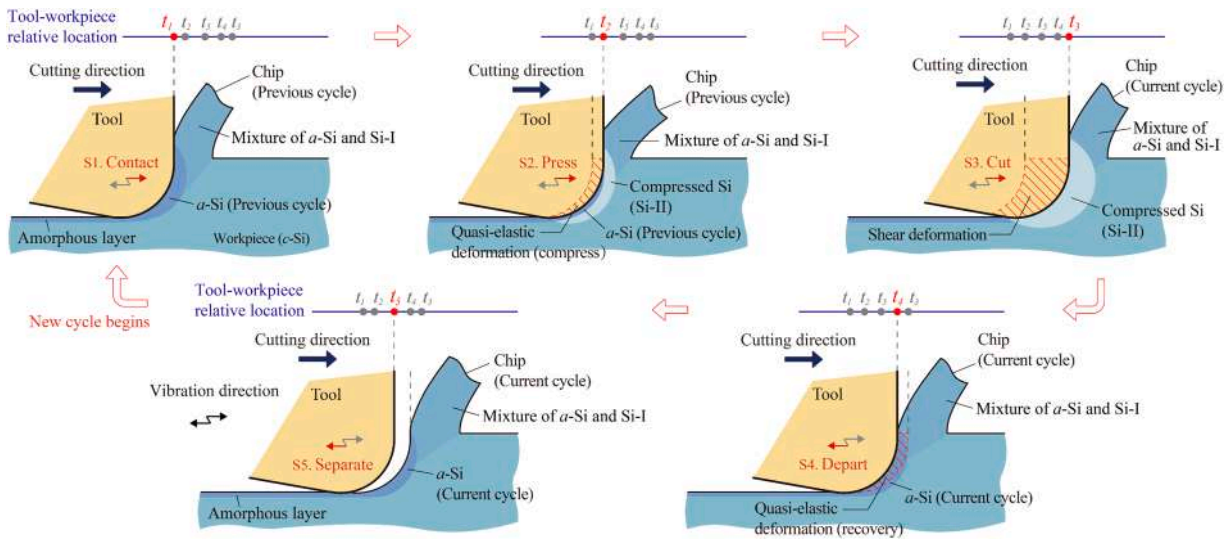

Fig. 14. Schematic model for the formation mechanisms of chips in one cycle of ductile vibration cutting of silicon.

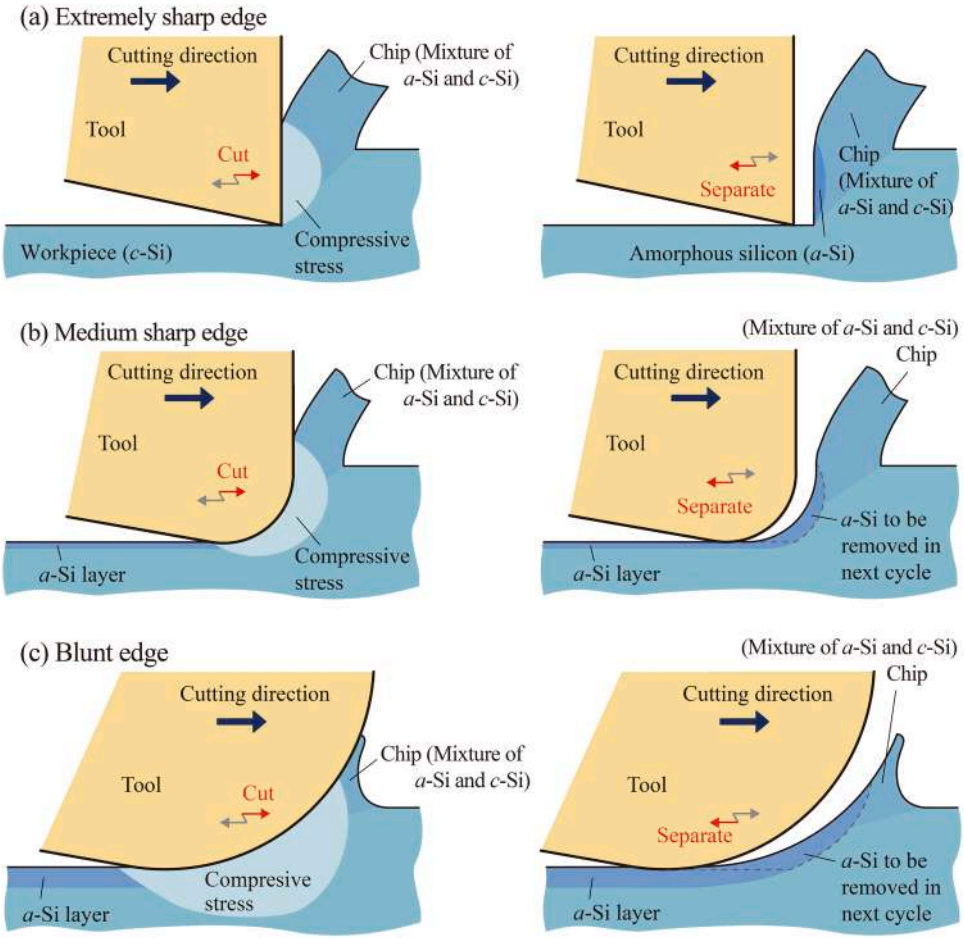

Fig. 15. Schematic models for the ductile vibration cutting of silicon by using tools with (a) extremely sharp edge, (b) medium sharp edge, and (c) blunt edge.

the tool edge contour well, while the cross-sectional profile of the vibration-cut groove is much shallower than the tool edge contour. With a further increase in the cut depth, complete material removal started to occur under the vibration-assisted cutting condition forming a normal vibration-cut groove. Fig. 11(h) shows the cross-sectional profiles of the two grooves far from the cut-in point. The profile of the vibration-cut groove is smooth and fits the tool-edge contour well. In contrast, the profile of the conventional cut groove is rough, which is caused by the microfractures generated on the groove surface, although the conventional cut groove has the same width as the vibration-cut groove. These results confirm that vibration cutting can increase the depth of cut for brittle-to-ductile transition in processing single-crystal silicon.

Additionally, these results indicate that if the depth of cut is extremely small (< 10 nm) during the vibration cutting process, the material is not removed as it would be in the conventional cutting process; instead, significant elastic deformation of the material occurs.

3.5. Subsurface microstructural changes of ultrasonic vibration cut microgrooves

The Raman spectra of the grooves machined under conventional and vibration-assisted conditions are shown in Fig. 12(a). The detection locations were chosen in the ductile-cut area of the grooves. The Raman peak at 520 cm^{-1}, indicating single-crystal silicon (*c*-Si), is the main peak in both spectra; but the intensity of the peak of *c*-Si in the vibration-cut groove is slightly lower than that in the conventional-cut groove. However, at the Raman shift of approximately 475 cm^{-1}, indicating amorphous silicon (*a*-Si), the corresponding intensity is slightly stronger in the vibration-cut groove. These results indicate that vibration cutting causes a greater extent of microstructural change in the workpiece subsurface.

In addition, the Raman spectra of cutting chips generated in the grooving process were also characterized, as shown in Fig. 12(b). The peak at 475 cm^{-1} associated with the amorphous phase and the peak at 520 cm^{-1} associated with crystalline Si are the main peaks. This result is consistent with the report from Yan et al. (2009a), indicating that the chips produced in the ductile cutting of silicon contain amorphous and crystalline silicon. Because the absolute Raman intensity was affected by the size and density of the chip cluster, Raman peak intensity ratio (r) was introduced to analyze the degree of amorphization in cutting chips, and determined by.

$$r = I_a/I_c \tag{6}$$

where I_a is the *a*-Si peak intensity and I_c is the *c*-Si peak intensity.

The results revealed that under conventional cutting conditions r was 1.097, while under vibration-assisted cutting conditions r was 1.179. The vibration-assisted cutting achieved 7.5% growth in the amorphous silicon, indicating that intermittent cutting promoted the amorphization of silicon, which is consistent with the cyclic indentation result that cyclic loading causes more amorphous phase formation in the material. The higher level of amorphous phase in the chips produced under vibration cutting may be because, on the one hand, as reported by Yan et al. (2009a) the Si-II phase in the chips will change to amorphous phase after the separation of chips and tool, which is like the amorphization occurring in unloading of indentation; on the other hand, the number of separations between the tool and material are increased due to vibration cutting, and the amorphous phase would be generated in the material and be removed as chips in the following cutting cycle.

4. Discussion of process mechanisms

4.1. Mechanism of cyclic indentation

Based on the subsurface microstructure characterizations (Section 3.1) and the analysis of the load-displacement curves and the curves of average contact pressure vs. displacement (Section 3.3), a model for the possible evolution of subsurface microstructural changes under cyclic nanoindentation is proposed, as illustrated in Fig. 13. In the first cycle, when the load reaches a maximum, the diamond cubic (Si-I) phase beneath the indenter changes into the metallic β-Sn (Si-II) phase as the pressure increases above 13 GPa. Then, as the indenter starts to withdraw from the material (unloading of the first cycle), the far-field transition with the elastic region undergoes elastic recovery first. As the indenter continues to withdraw, the pressure gradually decreases, and when the pressure falls below 9 GPa, the metallic β-Sn phase changes to the amorphous phase (*a*-Si), which causes the elbow event to occur in the unloading curve. In addition, nanocrystalline grains with Si-III/XII phases nucleate within the amorphous phase with random numbers and shapes; these nanograins tend to form in the central lower region of the indent where the highest pressure is generated, which has been observed using cross-sectional transmission electron microscope by Yan et al. (2005a). During the loading of the second cycle, the indenter first contacts the mixture of amorphous phase and nanocrystalline grains and deforms the material elastically, corresponding to stage 1 in the load-displacement curves and the AB region in the curves for average contact pressure (ACP). As the indentation depth continues to increase, the pressure reaches ~21 GPa, causing the amorphous phase to transform into Si-II phase. Thus, the indentation depth increases faster, and the contact pressure suddenly drops, which corresponds to stage 2 in the load-displacement curves and the BC region in the ACP curves. With further increase in the indentation depth, the increasing rate of the indentation depth slows down again, correlating with stage 3 in the load-displacement curves and the CD region in the ACP curves, because the phase transformation-based plastic deformation becomes weaker, and the elastic deformation becomes dominant again. When the load of the indenter exceeds the peak load of the previous cycle, the pristine diamond cubic phase in the deeper substrate changes to the Si-II phase, causing a faster increase in the rate of indentation depth and a decreased contact pressure, which corresponds to stage 4 in the load-displacement curves and the DE region in the ACP curves. In the next few cycles, the process of microstructural changes will follow the above process, but the amorphous layer becomes larger during the unloading of the cycles, as evidenced by the fact that the intensity of the amorphous peak in the Raman spectra (Fig. 5) and the width of stage 2 in the load-displacement curve (Fig. 8) increase with increasing indentation cycles.

After several cycles of indentation, when the indenter is unloaded again, nanocrystals of Si-XII, which serve as nucleation points, continue to grow in the Si-II phase as the number of cycles of unloading increases (Ruffell et al., 2007). When the Si-XII seeds grow to a certain level, once the pressure is below 7.8 GPa, the Si-II phase rapidly changes to the Si-XII phase, which is accompanied by volume expansion (Huang and Yan, 2015). This causes a pop-out event, as presented in Fig. 10(b). However, Ackland et al. (1994) found that the Si-XII phase becomes unstable when the pressure is below ~2 GPa, and then part of it is converted into the Si-III phase. Thus, the residual indent shows a mixture of Si-III and Si-XII phases. Then, during the loading of the next cycle, when the indenter reaches the peak load, the Si-III phase reverts to the Si-XII phase, and the Si-XII phase generated in the previous cycle persists because of its higher hardness than the Si-I phase; meanwhile, a thin layer of Si-I phase beneath the Si-XII phase will transform into the Si-II phase. Subsequently, unloading begins, during which the Si-II phase is reverted to the Si-XII phase owing to the existence of Si-XII phase seeds. However, the pop-out event becomes insignificant (see Fig. 9) because the amount of the newly formed Si-II phase is too small. When the pressure falls below ~2 GPa, a part of the Si-XII phase transforms to the Si-III phase again, and as the number of indentation cycles increases, an increasing amount of Si-XII phases tend to transform to the Si-III phase in the process of unloading, as suggested by the Raman results, which reveal that the number of C-type spectra with strong Si-III phase peaks increased with the number of indentation cycles.

From this evolution model, it is also possible to determine the reason for the phenomenon (Fig. 7) that crack growth is suppressed during the incremental cyclic loading of nanoindentations. In cyclic nanoindentation, the maximum load of each cycle gradually increased until it reached the ultimate peak in the last cycle. In single-cycle nanoindentation, the maximum load, which is also the ultimate peak, was applied to the workpiece surface in one cycle. It is obvious that the cracks generated in the early cycles of the cyclic nanoindentation will be smaller than those produced in the single-cycle nanoindentation owing to the smaller maximum load. Moreover, as amorphization occurs in the workpiece subsurface in the early cycles of cyclic nanoindentation and that the amorphous phase possesses better microplasticity and less

hardness (Yan et al., 2005a), the depth of the indent produced in cyclic indentation is much deeper than that produced in single-cycle indentation, but the crack length in cyclic indentation is shorter or slightly higher than that of single-cycle indentation.

4.2. Mechanism of UVC

Although both cyclic nanoindentation and vibration cutting generate a cyclic loading effect, the kinematics of material deformation during indentation and cutting are not exactly the same. In the former case, the material is deformed by pressing the indenter downwards, and compressive stress plays a significant role in material deformation; in the latter case, the material is separated from the substrate by moving the tool forward, and shear stress contributes greatly to material removal. Nonetheless, the phenomena observed in the cyclic nanoindentation test helps explain the machining mechanism of vibration cutting, because during vibration cutting of the material, the tool also generates cyclic compressive stress on the material, especially when the tool edge is blunt causing a low relative tool sharpness.

Based on the findings from cyclic nanoindentation tests and the widely accepted deformation mechanisms of silicon in conventional cutting, a model for the formation mechanisms of chips in one cycle of ductile vibration cutting of silicon was proposed, as illustrated in Fig. 14. As the tool approached the material (S1. Contact), the tool rake face first made contact with the amorphous zone, which was caused by the tool-workpiece separation (unloading) in the previous cutting cycle. Once the tool advanced into the material (S2. Press), a quasi-elastic deformation occurred within the amorphous zone because the amorphous phase was softer than the substrate; meanwhile, a phase change from a diamond cubic (Si-I) phase to a metallic (Si-II) phase was initiated in the material at a relative distance from the tool owing to the generated compressive stress. When the tool advanced further relative to the material (S3. Cut), the shear stress caused the material to separate from the substrate, resulting in chip formation. Therefore, the chips contain the amorphous phase generated in the previous cycle, the amorphous phase formed after unloading of the Si-II phase in the current cycle, and the shearing-induced material removal of the Si-I phase in the current cycle. Subsequently, the tool rake face began to depart from the material (S4. Depart), quasi-elastic recovery occurred at the tool-workpiece interface, and a new amorphous phase was generated in this region by the unloading of the Si-II phase. Finally, the tool and material were completely separated (S5. Separate). Subsequently, new cutting cycles were initiated.

In conventional cutting, the amorphous phase in the chips only forms after the chips have been separated from the substrate; however, in vibration cutting, the amorphous phase in the chips comprises not only the amorphous phase formed by the same process as conventional cutting, but also the periodic tool-workpiece separation-induced amorphous phase. Therefore, the extent of amorphization in the chip generated by vibration cutting was greater than that generated by conventional cutting, which is consistent with the measured Raman spectra of the chips. Besides, the tool obtains a higher instantaneous cutting speed and acceleration in ultrasonic vibration cutting than in conventional cutting. Therefore, on the one hand, in the tool-workpiece separation moment, the quick pressure release leads to formation of purer amorphous phase. On the other hand, in the tool-workpiece contact moment, compressive strength and dynamic fracture toughness of the amorphous phase are increased at higher strain-rate, as reported by Sheikh et al. (2018) and Li et al. (2020). And as a result, ductile mode machining of silicon is enhanced in the ultrasonic vibration cutting process.

If a tool with a blunt edge is used the shearing action becomes less significant during cutting and the plowing effect becomes significant; that is, the compressive stress-induced elastic and plastic deformation dominates the material deformation behavior, which consequently causes less material removal from the workpiece (Fang et al., 2005). A model for correlating the tool edge radius and the thickness of the plowed material was developed, as presented in the Appendix. This model indicates that the thickness of the plowed material increased with increasing tool edge radius. Thus, vibration cutting process with blunt-edge tools is closer to cyclic nanoindentation process. Moreover, in the conventional cutting of silicon, it has been reported that a blunt-edge tool can cause a thick amorphous layer to form in the workpiece subsurface, which changes from the high-pressure induced metallic phase after the tool has passed (unloading). Therefore, it is assumed that in the vibration cutting of silicon using a blunt-edge tool, a thicker amorphous layer would be generated than in conventional cutting because the tool vibration causes a cyclic compressive stress field under the tool, as illustrated in Fig. 15.

5. Conclusions

This study performed cyclic nanoindentation tests and vibration-assisted groove-cutting experiments on monocrystalline silicon. The surface morphologies and subsurface microstructures of residual indents and plunge-cut grooves were measured. A combined analysis of the cyclic nanoindentation test and groove-cutting experimental results was conducted to understand the material deformation behavior of the vibration cutting process. The following conclusions are drawn from this study:

(1) The material underwent significant plastic deformation during nanoindentation, resulting in plastic flow lines forming on the indented surfaces. The incremental cyclic loading of nanoindentation can suppress crack growth.
(2) Cyclic loading promotes microstructural changes in the subsurface material. In particular, for single-crystal silicon, as the number of loading cycles increases, the microstructure of the subsurface damaged layer tends to change from an amorphous phase to a mixture of bc8 and r8 phases. Moreover, the cyclic loading action decreases the critical load for transitioning the β-Sn phase to the bc8 and r8 phases.
(3) In cyclic nanoindentation, the material undergoes quasi-elastic deformation during the period from the unloading of the previous cycle to when the applied force reloads to a value equal to the peak load of the previous cycle in the current cycle. Therefore, during vibration cutting, the material may also undergo quasi-elastic deformation from the point when the tool moves backward relative to the material in the previous cycle to the point when the tool presses into the material to the previous relative separation point in the current cycle.
(4) Under vibration-assisted cutting conditions, the critical depth for the brittle-to-ductile transition of silicon is 135 nm, which is approximately three times the critical depth under conventional cutting conditions in the present groove-cutting experiments.
(5) During the vibration cutting process with an extremely small depth of cut (< 10 nm), the material is not removed as in the conventional cutting process; instead, the material undergoes significant elastic deformation.
(6) Vibration-assisted cutting results in a 7.5% increase in amorphous silicon in the cutting chips compared to conventional cutting. This is because the material undergoes numerous loading and unloading cycles of the tool during the vibration cutting process, and the amorphization of silicon occurs during the unloading period. The promotion of amorphous formation by vibration cutting contributes to the ductile machining of silicon.

The results of this study provide a reference for understanding the effects of cyclic loading on the chip formation mechanism and material deformation behavior during the vibration-cutting process. As the kinematics and dominant stress of nanoindentation are not exactly the same as those of vibration cutting, further investigation of the effect of cyclic shear stress on material deformation behaviors is required to

thoroughly explore vibration cutting mechanisms.

CRediT authorship contribution statement

Weihai Huang: Conceptualization, Methodology, Investigation, Data curation, Writing – original draft. **Jiwang Yan:** Conceptualization, Visualization, Supervision, Writing – review & editing.

Declaration of Competing Interest

The authors declare that they have no known competing financial interests or personal relationships that could have appeared to influence the work reported in this paper.

Data Availability

No data was used for the research described in the article.

Acknowledgements

This work has been partially supported by Japan Society for the Promotion of Science, Grant-in-Aid for Scientific Research (B), project number 21H01230. The authors would like to thank AMETEK Precitech Inc. for providing equipment supports. Thanks are also extended to Mr. Tomoyuki Takano and Mrs. Kawori Tanaka of Central Testing Center of Keio University for their technical assistance in nanoindentation tests and SEM observations.

Appendix

See Appendix Figs. A1 and A2 and Appendix (Table A1).

In nano-cutting, the cutting tool has a tool edge radius (r) that is comparable to the uncut chip thickness (h). Because of this tool edge radius, it is generally assumed that the work material within h will be physically separated at segment point S into two material flows in its transformation into a chip: the actual uncut chip thickness (h_u), i.e., the material above the stagnation point, which flows up along the rake face and forms the chip, and the minimum chip thickness (h_s), i.e., the material below the stagnation point, which is extruded downward into the workpiece and exhibits some elastic recovery after the tool passes, as reported by Fang et al. (2015) and Rahman et al. (2020). Fig. A1 illustrates a schematic of the behavior of material flow separation with the cutting tool. In particular, if the cutting tool has an ideal sharp tool edge (Fig. A1, a yellow profile superimposed over the blue profile of the real blunt edge), material removal will be accomplished by pure shearing, i.e., $h_u = h$, and $h_s = 0$. This situation corresponds to Merchant's model (Merchant, 1945). However, if the cutting tool has a larger edge radius, the thickness of the material deformed by plowing and sliding will become larger, i.e., h_s gradually approaches h, and h_u gradually approaches zero. Therefore, when calculating the thickness of the plowed material (δ), the plowing and sliding can be approximated as an elastic–plastic indentation of the cylinder on the workpiece, in which the indentation load is twice the thrust force (F_t) and acts at point C, and thus δ can be given by Rahman et al. (2017) as:

$$\frac{\delta}{\delta_{yield}} = 0.35 \times \left(\frac{2F_t}{P_{yield}}\right)^{\frac{3}{2}} + 0.65 \tag{A.1}$$

where δ_{yield} is the vertical displacement at the onset of plasticity and P_{yield} is the maximum force for elastic contact.

δ_{yield} is determined by

$$\delta_{yield} = 4.75\frac{x_{yeild}^2}{2r} \tag{A.2}$$

and P_{yield} is determined by

$$P_{yield} = \frac{\pi E w}{4r(1-\nu^2)}x_{yeild}^2 \tag{A.3}$$

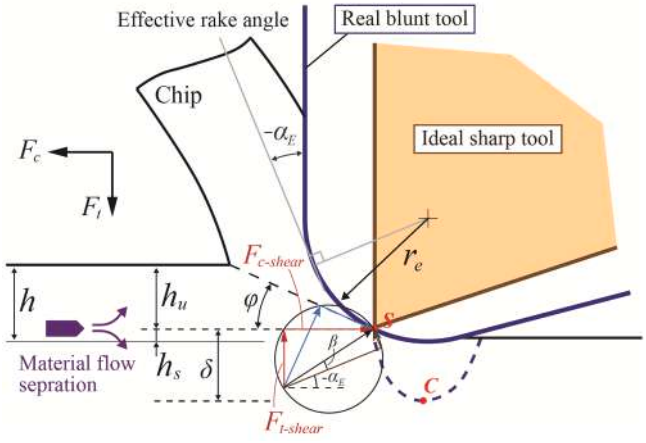

Fig. A1. Schematic of tool-workpiece contact in nano cutting.

where E denotes the elastic modulus of the workpiece. ν is the Poisson's ratio of the workpiece.

w is the width of the cut. For orthogonal cutting, w can be calculated as follows:

$$w = 2\sqrt{2Rh - h^2} \tag{A.4}$$

where R is the tool nose radius.

x_{yield} is the maximum half-contact length prior to the yield and can be determined as follows:

$$x_{yield} = \frac{2r(1-\nu^2)}{0.43E}\tau \tag{A.5}$$

where τ is the shear stress on shear plane.

According to the discussion in Fig. A1, when the effect of the tool-edge radius is considered in nano-cutting, the thrust force F_t can be expressed as

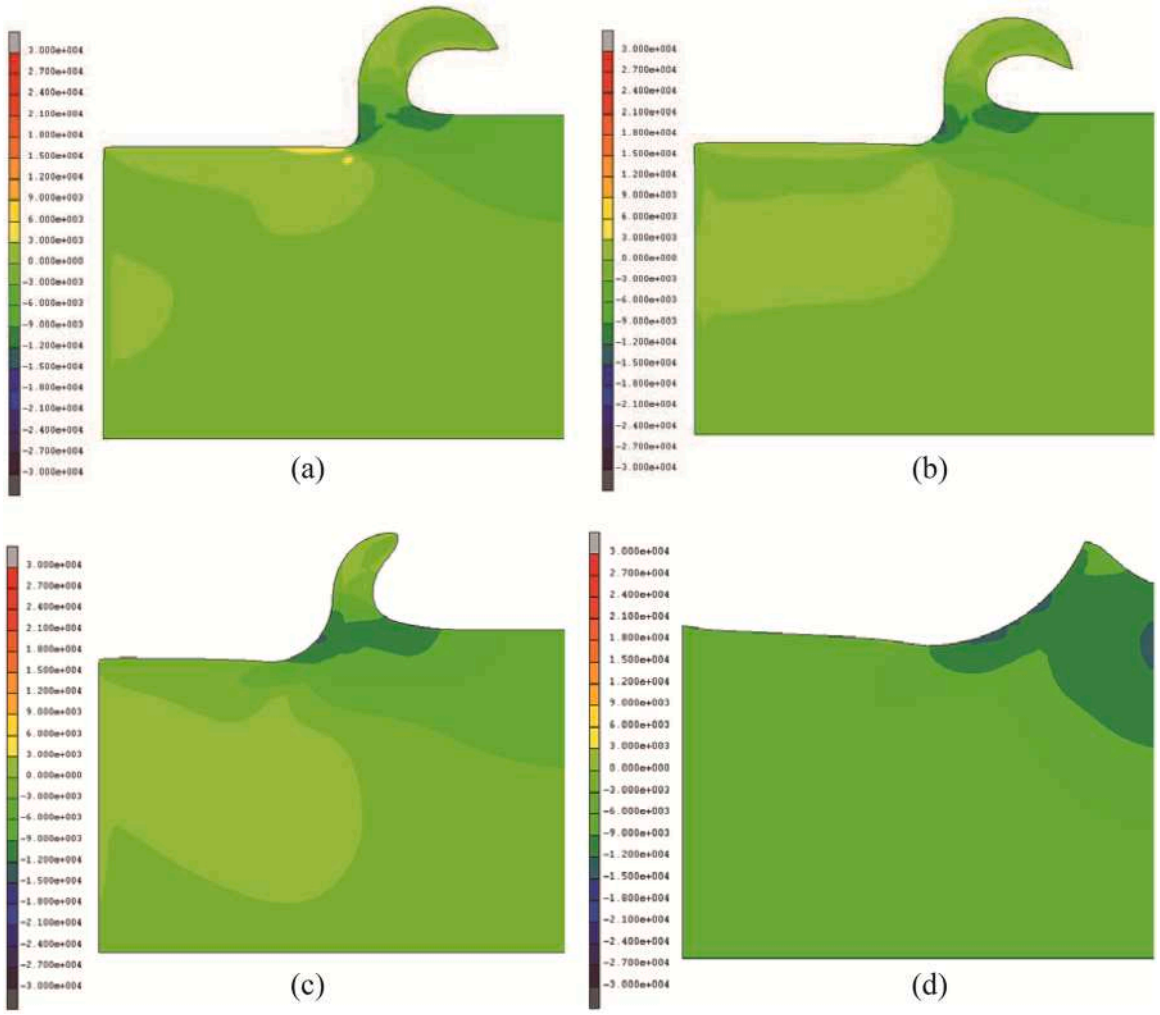

Fig. A2. The distribution of hydrostatic stress in the workpiece when using tools with different edge radii: (a) 50 nm, (b) 100 nm, (c) 200 nm, and (d) 500 nm (Yan et al., 2009b).

Table A1
Example of parameters used to estimate thickness of plowed material.

Elastic modulus E		160 GPa	
Poisson's ratio ν		0. 265	
Shear stress τ		6.5 GPa	
Tool nose radius R		1 mm	
Uncut chip thickness h		50 nm	
Friction angle β		20 Deg.	
Tool edge radius r	70 nm	100 nm	200 nm
Thickness of plowed material δ	114 nm	222 nm	610 nm

in Eq. (A.6), adopted from Waldorf et al. (1999):

$$F_t = F_{t-shear} + F_{t-plow} \tag{A.6}$$

where $F_{t\text{-}shear}$ is the thrust force component due to shearing and $F_{t\text{-}plow}$ is the thrust force component due to plowing and sliding.

The thrust-force component by shearing can be calculated using the expression given by Fang et al. (2015):

$$F_{t-shear} = \frac{\tau h_u w \cos(\beta - \alpha_E)}{\sin\varphi \cos(\varphi + \beta - \alpha_E)} \cdot \tan(\beta - \alpha_E) \tag{A.7}$$

where φ is the shear angle; according to the maximum shear stress criterion that the shearing generates in the direction of maximum shear stress, the shear angle can be estimated from Eq. (A.8), adopted from Merchant (1945):

$$\varphi = \frac{\pi}{4} - \frac{(\beta - \alpha_E)}{2} \tag{A.8}$$

where β is the friction angle. α_E is the effective rake angle (negative number) and can be calculated as follows:

$$\alpha_E = -\sin^{-1}(1 - h/r), \text{ for } h \le r(1 + \sin\alpha) \tag{A.9}$$

where α is nominal rake angle.

The thrust force component due to plowing and sliding can be obtained using an elastic-plastic model for cylinder indentation, adopted from Waldorf et al. (1999), as expressed in Eq. (A.10).

$$F_{t-plow} = \frac{\pi a^2 E}{4(1-\upsilon^2)r} \cdot l \tag{A.10}$$

where a is the half-width of the contact in the plowing zone in orthogonal cutting and can be estimated as follows:

$$a = \sqrt{2rh_s - h_s^2} \tag{A.11}$$

l is the contact length corresponding to the width of cut for plowing zone in orthogonal cutting and can be estimated using the following equation:

$$l = 2\sqrt{2Rh_s - h_s^2} \tag{A.12}$$

In the above equations, the shear stress τ, elastic modulus E, and Poisson's ratio ν are dependent on the materials; thus, they are assumed to be independent of the tool edge radius. The tool nose radius R and uncut chip thickness h are pre-determined cutting parameters. From Son et al. (2005) the minimum chip thickness h_s can be determined as follows:

$$h_s = r\left(1 - \cos\left(\frac{\pi}{4} - \frac{\beta}{2}\right)\right) \tag{A.13}$$

Therefore, in this modelling situation, the thickness of the plowed material is affected only by the tool edge radius r and friction angle β.

Table A1 lists the material properties of silicon and the predetermined cutting parameters. Here, β was simplified as a constant angle of 20°. Therefore, by substituting these values into the above equations, the thickness of the plowed material can be determined. The calculated results are listed in Table A1. It can be found that the thickness of plowed material δ increases with increasing tool edge radius r. This result also agrees with the result in the simulation study by Yan et al. (2009b) revealed that the hydrostatic stress distribution beneath the tool deepens when the tool edge radius increases, as shown in Fig. A2.

References

Ackland, G.J., Maclean, J.R., Piltz, R.O., Hatton, P.D., Pawley, G.S., Crain, J., 1994. Reversible pressure-induced structural transitions between metastable phases of silicon. Phys. Rev. B 50, 13043–13046.

Arefin, S., Zhang, X., Kumar, A.S., Neo, D.W.K., Wang, Y., 2021. Study of chip formation mechanism in one-dimensional vibration-assisted machining. J. Mater. Process. Technol. 291, 117022.

Bai, W., Wang, K., Du, D., Zhang, J., Huang, W., Xu, J., 2022. Design of an ultrasonic elliptical vibration device with two stationary points for ultra-precision cutting. *Ultrasonics 120*, 106662.

Chang, L., Zhang, L., 2009. Mechanical behaviour characterisation of silicon and effect of loading rate on pop-in: a nanoindentation study under ultra-low loads. Mater. Sci. Eng.: A 506, 125–129.

Chavoshi, S.Z., Gallo, S.C., Dong, H., Luo, X., 2017. High temperature nanoscratching of single crystal silicon under reduced oxygen condition. Mater. Sci. Eng.: A 684, 385–393.

Chen, Y., Cai, Y., Shimizu, Y., Ito, S., Gao, W., Ju, B., 2016. Ductile cutting of silicon microstructures with surface inclination measurement and compensation by using a force sensor integrated single point diamond tool. J. Micromech. Microeng. 26, 025002.

Domnich, V., Gogotsi, Y., 2002. Phase transformations in silicon under contact loading. Rev. Adv. Mater. Sci. 3, 1–36.

Domnich, V., Gogotsi, Y., Dub, S., 2000. Effect of phase transformations on the shape of the unloading curve in the nanoindentation of silicon. Appl. Phys. Lett. 76, 2214–2216.

Fang, F., Xu, F., Lai, M., 2015. Size effect in material removal by cutting at nano scale. Int. J. Adv. Manuf. Technol. 80, 591–598.

Fang, F.Z., Wu, H., Liu, Y.C., 2005. Modelling and experimental investigation on nanometric cutting of monocrystalline silicon. Int. J. Mach. Tools Manuf. 45, 1681–1686.

Fischer-Cripps, A.C., 2011. Nanoindentation, 3rd edition. Springer, New York, NY. https://doi.org/10.1007/978-1-4419-9872-9.

Fujisawa, N., Williams, J.S., Swain, M.V., 2007. On the cyclic indentation behavior of crystalline silicon with a sharp tip. J. Mater. Res. 22, 2992–2997.

Geng, H., Du, W., Wang, H., Li, J., 2021. Mechanical behavior in the interior and boundary of magnesium aluminate spinel (MgAl2O4) grain under nanoindentation. Appl. Opt. 60 6639–6647.

Gogotsi, Y.G., Domnich, V., Dub, S.N., Kailer, A., Nickel, K.G., 2000. Cyclic nanoindentation and raman microspectroscopy study of phase transformations in semiconductors. J. Mater. Res. 15, 871–879.

Guo, P., Ehmann, K.F., 2013. Development of a tertiary motion generator for elliptical vibration texturing. Precis. Eng. 37, 364–371.

Hayasaka, T., Sun, P., Jung, H., Mizutani, Y., Shamoto, E., 2021. Proposal of 'ImpEC (impact excitation cutting)' for realization of high-flexibility and high-efficiency micro/nano surface texturing. CIRP Ann. 70, 41–44.
Huang, H., Yan, J., 2015. On the mechanism of secondary pop-out in cyclic nanoindentation of single-crystal silicon. J. Mater. Res. 30, 1861–1868.
Huang, W., Yu, D., Zhang, X., Zhang, M., Chen, D., 2018. Ductile-regime machining model for ultrasonic elliptical vibration cutting of brittle materials. J. Manuf. Process. 36, 68–76.
Jang, J., Lance, M.J., Wen, S., Tsui, T.Y., Pharr, G.M., 2005. Indentation-induced phase transformations in silicon: influences of load, rate and indenter angle on the transformation behavior. Acta Mater. 53, 1759–1770.
Juliano, T., Gogotsi, Y., Domnich, V., 2003. Effect of indentation unloading conditions on phase transformation induced events in silicon. J. Mater. Res. 18, 1192–1201.
Juri, A.Z., Basak, A.K., Yin, L., 2022. In-situ SEM cyclic nanoindentation of pre-sintered and sintered zirconia materials. J. Mech. Behav. Biomed. Mater. 126, 105068.
Li, P., Chen, S., Xiao, H., Chen, Z., Qu, M., Dai, H., Jin, T., 2020. Effects of local strain rate and temperature on the workpiece subsurface damage in grinding of optical glass. Int. J. Mech. Sci. 182, 105737.
Liu, C., Zhang, J., Zhang, J., Chu, J., Chen, X., Xiao, J., Xu, J., 2021. Numerical investigation on material removal mechanism in elliptical vibration cutting of single-crystal silicon. Mater. Sci. Semicond. Process. 134, 106019.
Maroju, N.K., Jin, X., 2022. Effect of speed ratio on shear angle and forces in elliptical vibration assisted machining. J. Mater. Process. Technol. 302, 117498.
Merchant, M.E., 1945. Mechanics of the metal cutting process. II. Plasticity conditions in orthogonal cutting. J. Appl. Phys. 16, 318–324.
Moriwaki, T., Shamoto, E., Inoue, K., 1992. Ultraprecision ductile cutting of glass by applying ultrasonic vibration. CIRP Ann. 41, 141–144.
Nath, C., Rahman, M., Neo, K.S., 2011. Modeling of the effect of machining parameters on maximum thickness of cut in ultrasonic elliptical vibration cutting. J. Manuf. Sci. Eng. 133, 11007.
Nix, W.D., Gao, H., 1998. Indentation size effects in crystalline materials: a law for strain gradient plasticity. J. Mech. Phys. Solids 46, 411–425.
Pizani, P.S., Jasinevicius, R.G., Zanatta, A.R., 2006. Effect of the initial structure of silicon surface on the generation of multiple structural phases by cyclic microindentation. Appl. Phys. Lett. 89, 31917.
Rahman, M.A., Amrun, M.R., Rahman, M., Kumar, A.S., 2017. Variation of surface generation mechanisms in ultra-precision machining due to relative tool sharpness (RTS) and material properties. Int. J. Mach. Tools Manuf. 115, 15–28.
Rahman, M.A., Rahman, M., Mia, M., Gupta, M.K., Sen, B., Ahmed, A., 2020. Investigation of the specific cutting energy and its effect in shearing dominant precision micro cutting. J. Mater. Process. Technol. 283, 116688.
Ruffell, S., Bradby, J.E., Williams, J.S., Munroe, P., 2007. Formation and growth of nanoindentation-induced high pressure phases in crystalline and amorphous silicon. J. Appl. Phys. 102, 63521.
Sheikh, M.Z., Wang, Z., Suo, T., Li, Y., Zhou, F., Ahmed, S., Uzair, A.D., 2018. High rate response and dynamic failure of aluminosilicate glass under compression loading. Procedia Struct. Integr. 13, 1244–1249.
Son, S.M., Lim, H.S., Ahn, J.H., 2005. Effects of the friction coefficient on the minimum cutting thickness in micro cutting. Int. J. Mach. Tools Manuf. 45, 529–535.
Waldorf, D.J., DeVor, R.E., Kapoor, S.G., 1999. An evaluation of ploughing models for orthogonal machining. J. Manuf. Sci. Eng. 121, 550–558.
Wang, J., Liao, W., Guo, P., 2020a. Modulated ultrasonic elliptical vibration cutting for ductile-regime texturing of brittle materials with 2-D combined resonant and non-resonant vibrations. Int. J. Mech. Sci. 170, 105347.
Wang, J., Yang, Y., Zhu, Z., Wang, Y., Liao, W., Guo, P., 2020b. On ductile-regime elliptical vibration cutting of silicon with identifying the lower bound of practicable nominal cutting velocity. J. Mater. Process. Technol. 283, 116720.
Wang, Y., Wang, J., Chen, A., Kwok, N., Guo, P., 2020c. Structural coloration using face turning and variable tool vibration frequency. J. Manuf. Process. 56, 1392–1396.
Yan, J., Takahashi, H., Tamaki, J.I., Gai, X., Kuriyagawa, T., 2005a. Transmission electron microscopic observation of nanoindentations made on ductile-machined silicon wafers. Appl. Phys. Lett. 87, 211901.
Yan, J., Takahashi, H., Gai, X., Harada, H., Tamaki, J.I., Kuriyagawa, T., 2006. Load effects on the phase transformation of single-crystal silicon during nanoindentation tests. Mater. Sci. Eng.: A 423, 19–23.
Yan, J., Asami, T., Harada, H., Kuriyagawa, T., 2009a. Fundamental investigation of subsurface damage in single crystalline silicon caused by diamond machining. Precis. Eng. 33, 378–386.
Yan, J., Zhao, H., Kuriyagawa, T., 2009b. Effects of tool edge radius on ductile machining of silicon: an investigation by FEM. Semicond. Sci. Technol. 24, 75018.
Yan, X.Q., Huang, X.M., Uda, S., Chen, M.W., 2005b. Effect of heavy boron doping on pressure-induced phase transitions in single-crystal silicon. Appl. Phys. Lett. 87, 191911.
Zhang, J., Zhang, J., Cui, T., Hao, Z., Zahranie, A., 2017. Sculpturing of single crystal silicon microstructures by elliptical vibration cutting. J. Manuf. Process. 29, 389–398.
Zhang, J., Zhang, J., Liu, C., Chen, X., Xiao, J., Xu, J., 2020. Machinability of single crystal calcium fluoride by applying elliptical vibration diamond cutting. Precis. Eng. 66, 306–314.
Zhang, X., Senthil Kumar, A., Rahman, M., Nath, C., Liu, K., 2012. An analytical force model for orthogonal elliptical vibration cutting technique. J. Manuf. Process. 14, 378–387.